

Mixed Conduction in an N-Type Organic Semiconductor in the Absence of Hydrophilic Side-Chains

Jokubas Surgailis, Achilleas Savva, Victor Druet, Bryan D. Paulsen, Ruiheng Wu, Amer Hamidi-Sakr, David Ohayon, Georgios Nikiforidis, Xingxing Chen, Iain McCulloch, Jonathan Rivnay, and Sahika Inal*

Organic electrochemical transistors (OECTs) are the building blocks of biosensors, neuromorphic devices, and complementary circuits. One rule in the materials design for OECTs is the inclusion of a hydrophilic component in the chemical structure to enable ion transport in the film. Here, it is shown that the ladder-type, side-chain free polymer poly(benzimidazobenzophenanthroline) (BBL) performs significantly better in OECTs than the donor–acceptor type copolymer bearing hydrophilic ethylene glycol side chains (P-90). A combination of electrochemical techniques reveals that BBL exhibits a more efficient ion-to-electron coupling and higher OECT mobility than P-90. In situ atomic force microscopy scans evidence that BBL, which swells negligibly in electrolytes, undergoes a drastic and permanent change in morphology upon electrochemical doping. In contrast, P-90 substantially swells when immersed in electrolytes and shows moderate morphology changes induced by dopant ions. Ex situ grazing incidence wide-angle X-ray scattering suggests that the particular packing of BBL crystallites is minimally affected after doping, in contrast to P-90. BBL's ability to show exceptional mixed transport is due to the crystallites' connectivity, which resists water uptake. This side chain-free route for the design of mixed conductors could bring the n-type OECT performance closer to the bar set by their p-type counterparts.

charges throughout the channel enables OECT operation with gains higher than any relevant technology to date and driving voltages in the order of a few mVs.^[1] The high gains rendered OECTs favorable for detecting neural activity,^[4] biochemical species and events,^[5,6] and as building blocks of neuromorphic computing^[7] and printed electrochemical circuits.^[8] In accumulation (enhancement) mode OECTs, the channel is intrinsically non-conducting and becomes “doped” by the ions injected upon the application of a gate voltage (V_G). The ions stabilize the electronic charges simultaneously excited in the CP, creating polaronic and bipolaronic states. These stabilized charges can then be conducted across the channel as the drain bias (V_D) is applied. The reverse gate biasing extracts the ions from the bulk back into the electrolyte, and the polymer becomes de-doped. We characterize the steady-state characteristics of OECTs by measuring the channel current (I_D) while sweeping V_G and V_D , from


1. Introduction

The organic electrochemical transistor (OECT) is the most widely investigated and applied device type in organic bioelectronics.^[1–3] OECTs use conjugated polymer (CP) films in the channel interfacing directly with an electrolyte. The gate voltage induced coupling of electrolyte ions with electronic

which the transconductance (g_m) is obtained, which is the first and foremost figure of merit of an OECT, indicating its ability to transduce ionic-to-electronic signals. Besides the biasing conditions, g_m is determined by OECT channel geometry and CP's capability to facilitate mixed transport and the density of charge pairs. The OECT g_m equation in the saturation regime is expressed as:

J. Surgailis, Dr. A. Savva, V. Druet, Dr. A. Hamidi-Sakr, Dr. D. Ohayon, Dr. G. Nikiforidis, Prof. S. Inal
Biological and Environmental Science and Engineering Division
Organic Bioelectronics Laboratory
King Abdullah University of Science and Technology (KAUST)
Thuwal 23955-6900, Saudi Arabia
E-mail: sahika.inal@kaust.edu.sa
Dr. B. D. Paulsen, R. Wu, Prof. J. Rivnay
Department of Chemistry
Northwestern University
Evanston, IL 60208, USA

Dr. X. Chen, Prof. I. McCulloch
Physical Science and Engineering Division
KAUST Solar Center (KSC)
King Abdullah University of Science and Technology (KAUST)
Thuwal 23955-6900, Saudi Arabia
Prof. I. McCulloch
Department of Chemistry
Chemistry Research Laboratory
University of Oxford
Oxford OX1 3TA, UK
Prof. J. Rivnay
Simpson Querrey Institute
Northwestern University
Chicago, IL 60611, USA

 The ORCID identification number(s) for the author(s) of this article can be found under <https://doi.org/10.1002/adfm.202010165>.

DOI: 10.1002/adfm.202010165

$$g_m = \frac{Wd}{L} \mu C^* (V_G - V_T) \quad (1)$$

where W , L , and d are the channel width, length, and thickness, respectively, μ is the OECT electronic mobility of the channel, C^* is the volumetric capacitance, and V_T is threshold/turn-on voltage. A high g_m translates into local amplification, aimed when building biosensors.

For ion permeability and transport, hence for high g_m , the consensus is that the channel material should have a hydrophilic component. Most OECT polymers share similar backbones to those designed for organic field-effect transistors or photovoltaics yet employ polar side-chains to transport ions.^[2] A popular synthetic approach to render conjugated backbones (e.g., polythiophene,^[9] benzodithiophene,^[10] propylenedioxythiophenes,^[11] bithiophene-thienothiophene,^[12] and naphthalene tetracarboxylic diimide^[13,14]) hydrophilic has been grafting ethylene glycol (EG) side chains. Most of these CPs are hole-transporting (p-type), and only a few reports developed electron-transporting (n-type) polymers.^[2,15] Besides their scarcity, while certain treatments (solvent-induced aggregation or n-dopants) improved the performance of the existing n-type OECTs,^[16,17] they still lag behind the p-type analogs. The lack of high-performance n-type mixed conductors is grim for OECT applications that aim to monitor electron transfer processes such as glucose oxidation^[6] or cation movements such as during the activity of ion channel proteins.^[18] Their scarcity also limits applications in electrochemical energy storage^[9] and complementary circuits.^[20] The fundamental challenge of n-type polymer implementation is the instability of electronic charges in air and water, causing traps and low mobilities. The latter necessitates high electrochemical biases to populate a sufficient number of carriers in the lowest unoccupied molecular orbital (LUMO). However, the electrochemical window of water (<1 V) limits the extent to which CPs can be biased before they suffer from harmful electrochemical side products, restricting the operating range^[16,17,21,22] Synthesis of n-types with LUMOs deeper than −4 eV mitigates stability issues in ambient environment,^[21,23,24] yet the design of such materials remains extremely challenging.

As of now, there are only two types of n-type polymers for OECTs; one set of materials is based on a naphthalene-1,4,5,8-tetracarboxylic-diimide-bithiophene (NDI-T2) based donor–acceptor type backbone, and the other one is the ladder-type polymer poly(benzimidazobenzophenanthroline) (BBL). The chemical structure of these polymers is not alike, except that they both have a naphthalene frame, yet they are both OECT materials. The NDI-T2 based polymers were shown to operate in OECTs only if they had sufficient EG side-chain content.^[14] In contrast, despite the absence of EG side-chains or any specific polar units, BBL OECTs outperform these EG functionalized NDI-T2 polymers.^[20] Therefore, despite the recent advances in understanding OECT channel materials and mixed conduction, the chemical design principles for n-type mixed conductors remain unclear. Besides, polar side chain engineering, considered almost a necessity for OECT materials design, maybe less advantageous than envisaged. The main task of the hydrophilic side chains is to allow water/ion uptake and facilitate ion transport inside the water-swollen CP.^[14,25] Swelling, however, led to

undesired side effects such as loss of electronic mobility and possible film degradation for p-type CPs.^[25–29] The studies hypothesized that swollen amorphous regions disconnected regions of the film responsible for electronic charge transport. Excess swelling led to poor stability due to mechanical stress. Reducing swelling of poly(3,4-ethylenedioxythiophene):polystyrene sulfonate films through the addition of a crosslinker improved the film mechanical stability but at the cost of both electronic and ionic conductivity.^[30] This seemingly inherent trade-off can be circumvented entirely by avoiding the use of polar components altogether if the chains are connected in a way that facilitates ion transport while preserving lateral electron transport.

In this study, we construct new design rules for next-generation n-type CPs for bioelectronics. We systematically investigate and compare the electrochemical charging behavior and OECT performance of two n-type polymers, that is, BBL and a copolymer based on NDI-T2 backbone bearing EG side chains (named as P-90). We selected these two CPs as they perform well in aqueous electrolyte gated OECTs despite the significant differences in their backbone and although only one of them bears polar side chains. P-90 was selected as the representative of CPs with polar side chains as it was shown to swell substantially while exhibiting a higher OECT performance than its fully glycolated analogue.^[14] We find that BBL has around one order of magnitude higher OECT mobility than P-90 due to an edge-on backbone orientation and tighter packing, as gleaned from grazing incidence wide-angle X-ray scattering (GIWAXS) studies. Electrochemical UV–vis spectroscopy and cyclic voltammetry studies evidence that BBL has an earlier onset potential for electrochemical doping and generates more charges at comparable biasing conditions. Electrochemical impedance spectroscopy (EIS) measurements show that BBL has nearly three times higher C^* than P-90. Importantly, BBL does not swell in the electrolyte in the absence of bias. During electrochemical doping, it, however, swells more than P-90, revealed using electrochemical quartz crystal microbalance with dissipation monitoring (EQCM-D). In situ atomic force microscopy (AFM) measurements show that the morphological changes caused by electrolyte uptake during varying doping conditions are more drastic and irreversible for BBL. Yet, ion/water uptake minimally affects the crystallite structure. Our findings suggest that the rod-like, rigid BBL chains self-assemble into an architecture that enables short contacts that maintain high electron mobility while generating ion-permeable regions (envisaged as nano-voids). Lastly, besides its excellent steady-state performance, the BBL OECTs developed in this study exhibited faster response times than the previously reported devices,^[20] pushing BBL to the front line as an n-type OECT material. Our results argue that a particular hydrophilic phase is not required for hydrated ion transport as long as the polymer microstructure allows free volume for ion penetration.

2. Results

2.1. Electrochemical Reduction and the Ion-to-Electron Coupling

The chemical structures of BBL and P-90 are shown in Figure 1a. To monitor the electronic states generated in the

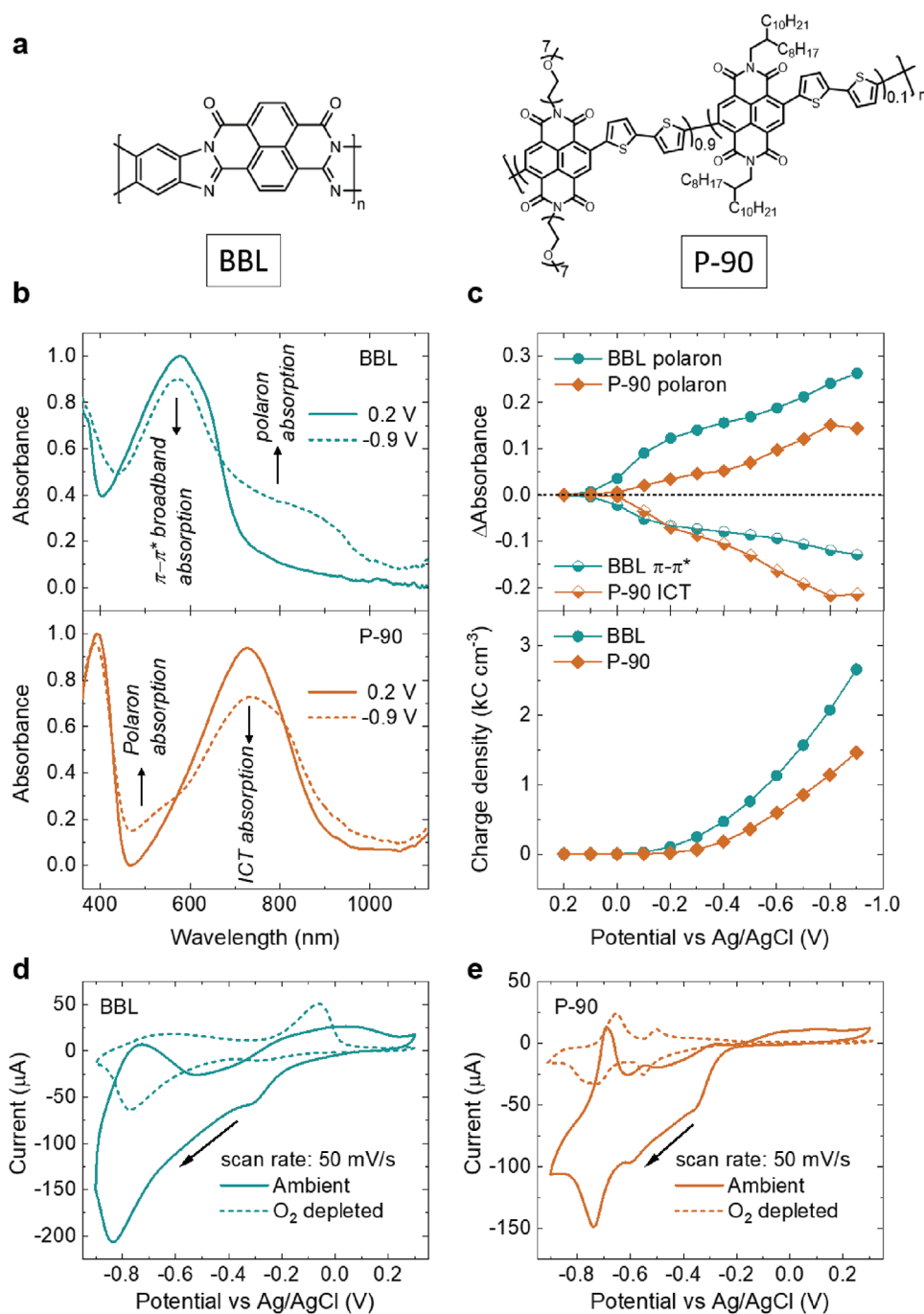


Figure 1. a) The chemical structures of BBL and P-90. b) Absorption spectra of BBL (top) and P-90 (bottom) films in a de-doped (solid line, 0.2 V vs Ag/AgCl) and doped state (dashed line, -0.9 V vs Ag/AgCl), c) absolute changes in polaron absorption, $\pi-\pi^*$ absorption and the ICT absorption of the films versus applied bias (top) and charge density of the films versus applied bias (bottom). Cyclic voltammetry curves of d) BBL and e) P-90 films recorded in ambient (solid lines) and in O₂-depleted environment (dashed lines).

films upon penetration of anions, we first performed electrochemical UV-vis spectroscopy measurements when the films were immersed in NaCl (0.1 M) and electrochemically reduced or oxidized using an Ag/AgCl electrode. Figure S1, Supporting Information shows the evolution of the spectra of the films at various biasing conditions. Figure 1b demonstrates the absorbance spectra of these films in two selected conditions,

electrochemically neutral (or de-doped) and reduced state obtained when the films were biased at 0.2 and -0.9 V versus Ag/AgCl, respectively. In the neutral state, the BBL spectrum shows a strong absorption peak around 570 nm, associated with the $\pi-\pi^*$ transition. Upon electrochemical doping, the intensity of this peak is slightly reduced while a new and broad band is formed in the wavelength range of 700 to 950 nm, associated

with the polaron transition.^[20,31] P-90 spectrum shows one absorption peak around 400 nm, ascribed to the π - π^* transition, and a second broader feature around 730 nm which is attributed to the intramolecular charge transfer (ICT) between the donor-acceptor moieties. P-90 spectrum exhibits a reduction in the ICT band accompanied with an increase in the polaron absorption at ≈ 430 nm,^[13,14,16] appearing within a narrower spectral range compared to BBL. The narrower polaron band of P-90 is attributed to the charge being mainly localized on the NDI moiety. In contrast, the charge is delocalized in the BBL monomer as well as extending to adjacent units, indicated by the broader spectral features generated at lower energies compared to P-90.^[31] In Figure 1c, top, we show the changes in the intensity of these absorption features as a function of applied bias. The spectral changes start occurring at lower voltages for BBL compared to P-90, indicating an earlier doping onset. The spectra also show more pronounced doping in BBL as the increase in polaron absorption at -0.9 V is almost double that of P-90. In Figure 1c, bottom, we observe the same trend in the amount of injected charge, as well as its onset, recorded simultaneously with the absorbance spectra. Note that both BBL and P-90 end up facilitating high Faradaic currents, meaning the calculated charge cannot be trivially ascribed to just electrochemical doping. We come to this conclusion by comparing cyclic voltammetry curves performed in ambient and O_2 -depleted environments in Figure 1d,e, which show a significant contribution to the current from oxygen reduction reaction (ORR). By comparing the highest peak reduction current values in ambient and O_2 -depleted environments, we find that around 2/3 and 4/5 of reduction current in BBL and P-90, respectively, is due to ORR.

Next, we used EQCM-D to elucidate the amount of mass loaded in the films during electrochemical doping. EQCM-D provides a means to correlate the combined weight of ions and water being injected into polymer films to the charge generated during biasing, thus, an estimate for ion-to-electron coupling efficiency.^[32] At first, we measure the EQCM-D signals of both films in air (Figure S2, Supporting Information and Figure 2a, step 1). These films are then exposed to O_2 -depleted electrolyte which leads to passive swelling (Figure 2a, step 2). In the absence of bias and upon exposure to the electrolyte, BBL shows very little (passive) swelling compared to P-90 (3% vs 38%, respectively). Once we apply a doping potential, both materials show a drastic increase in their mass (Figure 2a, step 3). At a voltage at -0.5 V versus Ag/AgCl, BBL swells by an additional 63% compared to the 14% of swelling by P-90. Figure 2b summarizes the relative swelling percentages of the films after exposure to the electrolyte and the application of a doping potential.

While these measurements suggest that the mass loaded upon doping is higher for BBL compared to P-90, it is not yet clear whether this mass can solely be attributed to dopant Na^+ ions as water may also be dragged into films along with ions.^[26] We thus performed additional EQCM-D experiments, which involved three reduction cycles in a potential window between 0.3 and -0.5 V versus Ag/AgCl. The mass taken up during these cycles and the corresponding currents recorded are shown in Figure 2c. As observed in the single-pulsing measurements, BBL loads more mass and generates higher

reduction currents compared to P-90. Figure 2d shows the mass and charge injected into the unit film volume increase with doping bias. Considering the earlier reduction onset of BBL (Figure 1d,e), even when we compare the swelling for BBL at lower doping potentials (e.g., -0.3 V vs Ag/AgCl) and P-90 at higher potentials (e.g., -0.5 V vs Ag/AgCl), BBL shows larger swelling than P-90. Using the charge density data and Faraday's law of electrolysis, we calculated the Na^+ mass density, assuming that one Na^+ ion couples with one electron in the film (see the analysis described in detail in the Experimental Section). The mass increase that Na^+ ions should cause is lower than the actual mass uptake. The extra mass on the films is thus attributed to water. Figure 2e shows that during doping, both films take more water than cations, suggesting that cations bring water along with them. The density of Na^+ ions and water molecules injected into the film is higher for BBL compared to P-90. However, when we look at the ratio of water/ Na^+ taken up at each doping potential, we see that for P-90, at voltages below -0.4 V, more water is dragged into the film for each dopant ion (Figure S3, Supporting Information). Therefore, for P-90, while the number of ions taken up is lower, these ions bring more water along, especially at low doping potentials.

2.2. OECT Characteristics

As we verified the superior charging ability of BBL over P-90 and discovered that both films uptake substantial amount of water during charging in aqueous electrolytes, we next evaluated the performance of microscale n-type OECTs comprising these polymers at the channel. The channels we fabricated had a width of 100 μm and a length of 10 μm . OECT transconductance (g_m) and drain current (I_D) scale with the thickness of the films in the channel; hence we ensured the channel thicknesses were comparable for all films studied. Figure 3a,b shows a cross-sectional view and wiring of the OECTs, and the microscope images of channels spin-cast from representative solutions. Typical current-voltage characteristics of the devices can be found in Figure S4, Supporting Information. The transfer curves in Figure 3c show that the BBL channels reach an average I_D of 13.47 μA at $V_D = V_G = 0.6$ V, which is more than 70 times higher than the ≈ 0.18 μA recorded for the P-90 channels. Similarly, g_m reaches a maximum value of around 65.1 μS for BBL ($V_D = V_G = 0.6$ V) while it remains around 0.78 μS ($V_D = 0.6$ V) at $V_G = 0.5$ V for P-90 and drops to 0.51 μS at $V_G = 0.6$ V (Figure 3c). We calculate the geometry normalized g_m values in Figure S5a, Supporting Information. BBL exhibits the highest value of 0.815 $S cm^{-1}$, which is over 90 times greater than the g_m determined for P-90 (0.009 $S cm^{-1}$). Our micron-scale BBL OECTs have higher performance than the spray-coated BBL OECT (0.3 $S cm^{-1}$) reported by Sun et al.^[20]

Using Equation (1), we can now decouple the main terms contributing to the observed difference in device performance: the mobility (μ) and the volumetric capacitance (C^*) of the channel and the voltage overdrive ($V_G - V_T$). The threshold voltage (V_T), determined from the $\sqrt{I_D}$ versus V_G curves (Figure S5b, Supporting Information), is 0.19 V for BBL and 0.24 V for P-90. These V_T values correlate well with the onset

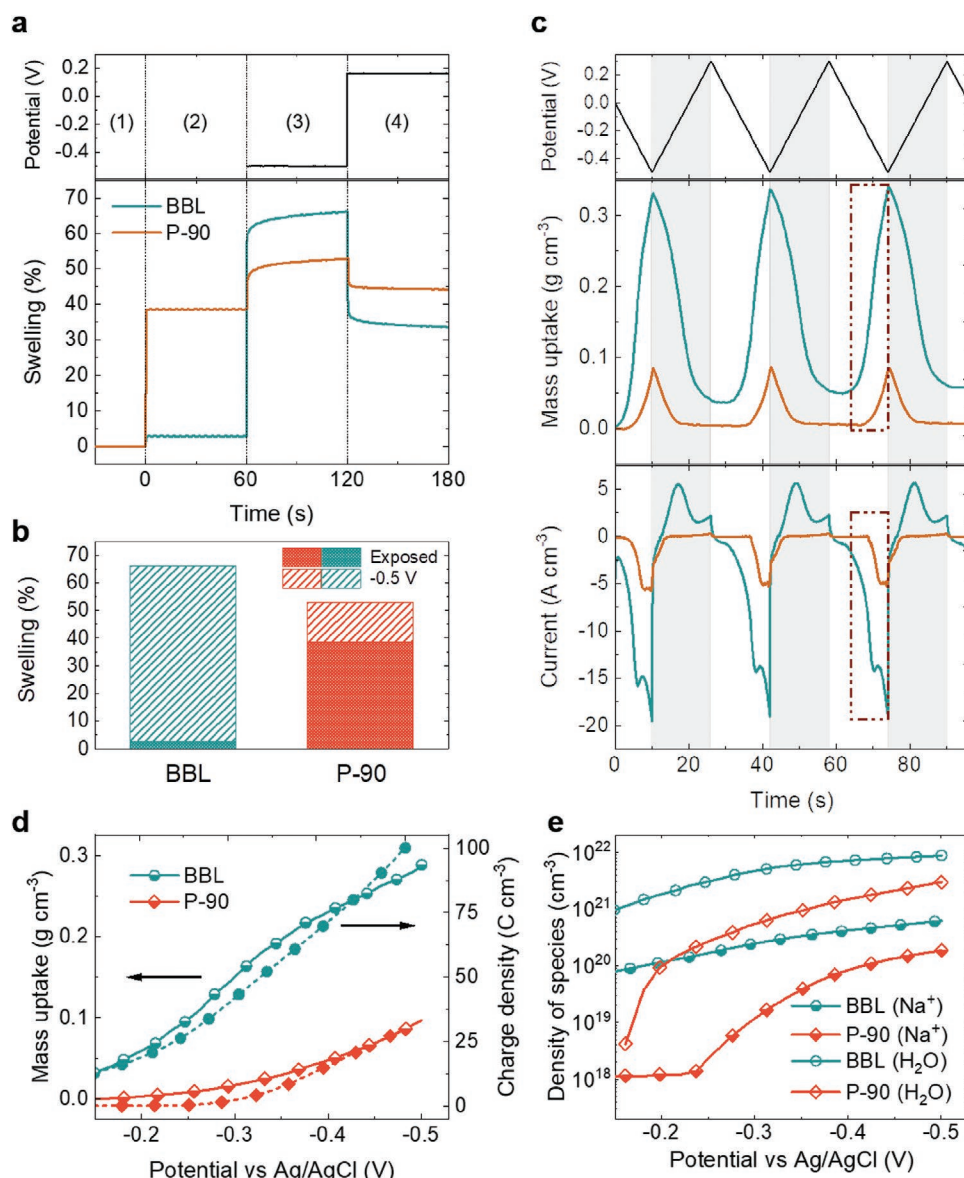


Figure 2. a) BBL and P-90 thin film characterization during 4 states: 1) dry state in air; 2) wet state in NaCl_(aq) 0.1 M with no external potential bias; 3) wet state in NaCl_(aq) 0.1 M under a doping bias (-0.5 V vs Ag/AgCl); 4) wet state in NaCl_(aq) 0.1 M under a dedoping bias back to open circuit potential (+0.16 V vs Ag/AgCl). Top: A doping and dedoping potential is applied for 60 s (step 3 and 4, respectively). Bottom: Polymer film swelling percentage caused by exposure to electrolyte (step 2) and a doping potential (step 3), as well as de-swelling caused by a dedoping potential (step 4). b) Total swelling percentage of the films in wet state with no external potential bias (exposed) and under -0.5 V versus Ag/AgCl. c) BBL and P-90 thin film characterization using cyclic voltammetry (CV) coupled with gravimetry. Top: Voltage profile of 3 CV cycles; the colored sections indicate the backward cycles. Middle: Mass uptake (and removal) of both films. Bottom: Current profiles of the films during CV cycles. Red box highlights the region for which charge and mass density calculations were made. d) Density of mass uptake (hollow symbols) and charge injected into the films (full symbols) as a function of applied voltage. e) Calculated density of Na⁺ and H₂O species injected into the films as a function of applied voltage. All EQCM-D measurements were performed with de-oxygenated electrolytes.

voltage for the changes in UV-vis spectra and the reduction onset observed in CV curves (Figure 1). By substituting the dimension and voltage factors into the equation, we plot the calculated μC^* versus V_G curves in Figure 3d. The μC^* product corresponding to the maximum g_m ($V_G = 0.6$ and 0.5 V, for BBL and P-90, respectively) is $1.99 \text{ F cm}^{-1} \text{ V}^{-1} \text{ s}^{-1}$ for BBL and $3.43 \times 10^{-2} \text{ F cm}^{-1} \text{ V}^{-1} \text{ s}^{-1}$ for P-90. μC^* product contributes by a factor of 58 toward the higher performance in BBL at biasing conditions that lead to highest transconductance.

Next, we decouple the μC^* product into its components. Performing EIS measurements with varying film geometries (Figure S6, Supporting Information), we generated capacitance versus polymer volume plots (Figure 3e). C^* extracted from the slope of the linear fit to these plots yield a C^* value of 731 F and 261 F cm^{-3} , for BBL and P-90, respectively. We then determined the OECT mobilities using an impedance matching technique based on Bernard's model.^[33,34] μ is $2.15 \times 10^{-3} \text{ cm}^2 \text{ V}^{-1} \text{ s}^{-1}$ for BBL and $7.45 \times 10^{-5} \text{ cm}^2 \text{ V}^{-1} \text{ s}^{-1}$ for P-90 (Figure 3f). Multiplying

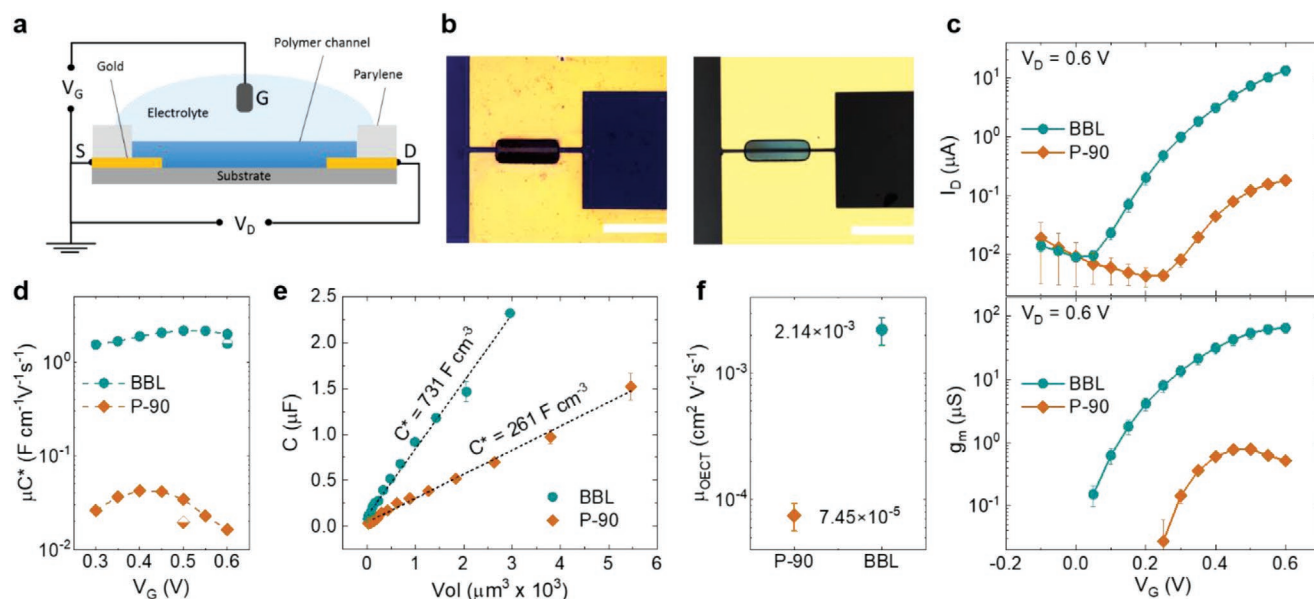


Figure 3. a) OECT schematics and wiring; S, D, and G represent source, drain, and gate (Ag/AgCl) electrodes, respectively. b) OECTs fabricated in this work had a width (W) of 100 μm , length (L) of 10 μm , as shown in the microscope images (left: BBL, right: P-90), and average film thickness (d) was 80 and 87 nm for BBL and P-90, respectively. The scale bar is 100 μm . c) Drain current (I_D) (top) and transconductance (g_m) (bottom) versus gate voltage (V_G). d) The μC^* product calculated from transconductance versus V_G curve (filled symbols) using Equation (1). The two data points (half-filled symbols) were calculated from independent measurements shown in (e) and (f). e) The dependence of film capacitance on its geometry. The capacitance was determined at 0.1 Hz from impedance spectroscopy measurements performed at -0.5 V versus Ag/AgCl. f) OECT electron mobility (μ_{OECT}) obtained from transconductance-frequency response measurements recorded at $V_D = 0.6$ V and $V_G = 0.6$ V for BBL and $V_G = 0.5$ V for P-90. In all measurements, the electrolyte was NaCl(aq) 0.1 M. The error bars were obtained from 4 or 6 OECTs.

these two independently measured capacitance and mobility values yields μC^* products of $1.57 \text{ F cm}^{-1} \text{ V}^{-1} \text{ s}^{-1}$ for BBL and $1.95 \times 10^{-2} \text{ F cm}^{-1} \text{ V}^{-1} \text{ s}^{-1}$ for P-90, which gives a $\mu C^*_{\text{(BBL)}}/\mu C^*_{\text{(P-90)}}$ ratio of 80.5, close to the calculated ratio of 58 that we obtained from the OECT measurements. Lastly, one of the commonly quoted drawbacks of the BBL OECT is its slow response time due to slow ion diffusion into the film.^[20] Our transient measurements revealed an OECT switch-on time of 5.2 ms for BBL, shorter than that of P-90, if not, comparable (Figure S7, Supporting Information). We summarize the OECT characteristics and materials figures of merit in Table 1.

2.3. Morphology and Film Microstructure—Impact of Doping

The superior OECT performance of BBL over P-90 came as a surprise as 1) the polymer does not have a particular hydrophilic phase to promote ion transport, and 2) the film uptakes

substantial water during doping, an excess of which has been shown to be detrimental for p-type OECT performance (particularly for μ).^[25,26] To investigate the particular morphology and microstructure to give such OECT performance to BBL, we performed AFM, transmission electron microscopy (TEM) and GIWAXS studies. To monitor the morphology evolution of the films in different doping states, AFM and GIWAXS were also conducted in operando or ex situ. Figure S8, Supporting Information reveals very different dry morphologies for the two polymers. While P-90 exhibits a typical fibrillary topography,^[35] BBL has features clumped into islands of varying sizes. These islands are distributed across the surface in an inhomogeneous manner with smaller clusters appearing between them, similar to the observations of Quintino et al.^[36] and Babel et al.^[37] AFM phase images of BBL films show nanoscale sheets in the range of 50–125 nm that are randomly oriented within the film, similar to previous reports.^[37,38] P-90 film appears smoother with an even distribution across the surface. In the TEM images,

Table 1. A summary of OECT parameters and electrochemical properties.

	V_T^a [V]	On/off ratio ^{b)}	$\frac{g_m^d}{(Wd/L)}$ [S cm^{-1}]	$\mu C^*_{\text{d)}$ [$\text{F cm}^{-1} \text{ V}^{-1} \text{ s}^{-1}$]	$C^*_{\text{e)}$ [F cm^{-2}]	μ_{OECT}^f [$\text{cm}^2 \text{ V}^{-1} \text{ s}^{-1}$]	$\mu C^*_{\text{g)}$ [$\text{F cm}^{-1} \text{ V}^{-1} \text{ s}^{-1}$]	$\tau_{\text{(ON)}}^h$ [ms]
BBL	0.19	1600	0.815	1.99	731	2.14×10^{-3}	1.57	5.2
P-90	0.24	19.4	9×10^{-3}	3.43×10^{-2}	261.5	7.45×10^{-5}	1.95×10^{-2}	41

^{a)} Obtained from the slope of the $\sqrt{I_D}$ versus V_G curve; ^{b)} Obtained by calculating $I_{D,V_G=0.6 \text{ V}}/I_{D,V_G=0 \text{ V}}$; ^{c)} Calculated by dividing the average g_m with the average channel dimensions; ^{d)} Calculated by dividing the maximum g_m with channel geometry Wd/L and overdrive voltage ($V_G - V_T$); ^{e)} Obtained from EIS measurements for various electrode dimensions; ^{f)} Calculated from g_m versus frequency (bandwidth) bandwidth measurements; ^{g)} Calculated by multiplying the independently measured μ_{OECT} and C^* values; ^{h)} OECT switch on time obtained from pulsed response time measurements.

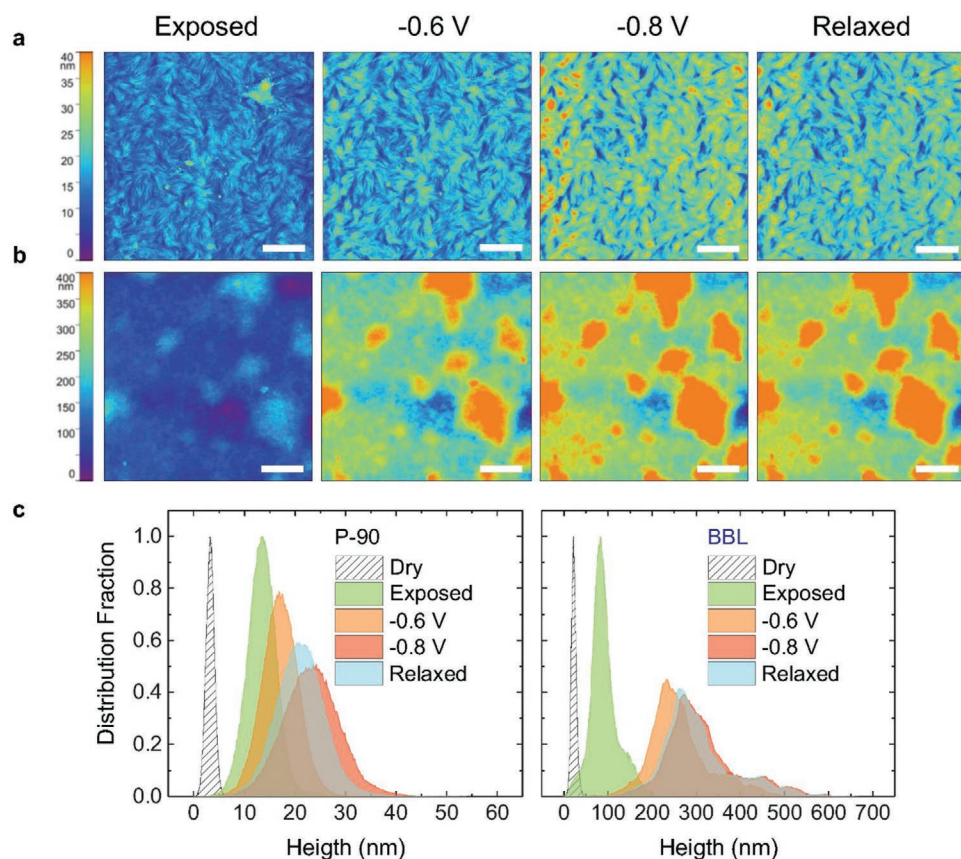


Figure 4. AFM images ($10 \times 10 \mu\text{m}$) of n-type films a) P-90 and b) BBL. The films were immersed in 0.1 M NaCl at different conditions: neutral state (exposed to electrolyte with no bias), doped state at -0.6 V versus Ag/AgCl, doped state at -0.8 V versus Ag/AgCl and de-doped back to neutral state. The scale bar is $2 \mu\text{m}$. c) Height distribution curves for P-90 and BBL extracted from the AFM images taken during these four conditions as well as dry state ($1 \times 1 \mu\text{m}$).

P-90 shows a smooth, fibrillar structure as observed in AFM, while BBL appears to be much more jagged/flaky and disconnected on smaller scales (Figure S9, Supporting Information).

When immersed in 0.1 M NaCl solution (images tagged as “Exposed”), P-90 appears relatively flat with a root mean squared (RMS) roughness of 3 nm and an average height difference of 13.5 nm. (Figure 4a, see Table S1, Supporting Information for RMS values). The topography exhibits typical fibrillary structures seen in dry state. When we analyze the height distribution on the P-90 surface, we find that it is close to a perfect Gaussian shape centered on 13.5 nm (Figure 4c, left). On the other hand, BBL has a higher RMS roughness of 31.9 nm and an average height difference of 92.1 nm (Figure 4b, Table S1, Supporting Information). BBL has a broad height distribution reflecting its rough surface peaking at $\approx 83 \text{ nm}$ (Figure 4c, right).

Upon injection of cations at -0.6 V , both polymer films swell, and as the voltage increases, so does the size of the features (Figure 4a,b). The P-90 height distribution now has a new and broadened peak distribution at 16.9 and 23.2 nm upon doping at -0.6 and -0.8 V , respectively (Figure 4c). Film surface roughness increases slightly toward 3.6 and 5.6 nm, respectively (Table S1, Supporting Information). After dedoping the film back to neutral state, the distribution center is shifted to 21 nm, while roughness decreases to 4.7 nm, indicating semi-reversible

morphological changes for P-90 upon electrochemical doping. BBL, on the other hand, undergoes these morphological changes much more drastically (Figure 4b). First, the surface features become larger. The height distribution profile has now a three times larger sized peak, 234 and 281 nm at -0.6 and -0.8 V , respectively (Figure 4c). Film surface roughness increases more than double its original value, reaching 68.2 and 82.7 nm at -0.6 and -0.8 V , respectively (Table S1, Supporting Information). Second, after the films are relaxed back to neutral state, both the distribution center and roughness remain almost the same. These results agree with the substantial swelling of BBL with water (as well as ions) upon doping that we observed in EQCM-D measurements and the large mass remaining in the film upon dedoping.

The changes that BBL morphology undergoes upon interaction with electrolyte ions are substantial and irreversible. We thus sought to understand the impact of doping on crystallites and collected 2D GIWAXS patterns from the dry films, films that had undergone ex situ electrolyte exposure, electrochemical doping, and electrochemical dedoping, as shown in Figures S10 and S12, Supporting Information. BBL thin films take on an edge-on packing motif with π -stack (010) scattering occurring in-plane and lamellar scattering (h00) occurring out-of-plane (Figure S12, Supporting Information). In contrast, P-90 takes

on a predominately face-on packing motif, consistent with previous NDI-T2 polymers,^[14,39–41] with π -stack scattering occurring out-of-plane and lamellar scattering occurring both in- and out-of-plane. P-90 has significant order along the backbone, as evidenced by strong backbone scattering (Figures S11 and S13, Supporting Information). Though backbone scattering is absent in BBL films, significant order along the backbone direction can be inferred from BBL's ladder structure and the tendency of BBL to form long nanobelts following the [001] direction.^[42]

Ex situ BBL molecular packing was astonishingly similar to the as cast BBL films regardless of electrolyte exposure, electrochemical doping, or electrochemical dedoping, as shown in Figure S12, Supporting Information. As a comparison, BBL doped molecularly using tetrakis(dimethylamino)ethylene shows a large shift of the lamellar scattering peak, implying a lamellar d-spacing expansion of $\approx 75\%$.^[31] Here, following aqueous electrochemical doping, the BBL shows a minimal lamellar expansion of 0.1 Å, and π -stack contraction of 0.05 Å. The π -stack contraction is reversible upon electrochemical dedoping, while the lamellar expansion is not. The ex situ measured BBL lamellar spacing (even as cast) is such that intercalation and retention of unsolvated cations is geometrically possible. GIWAXS is not sensitive to swelling in the amorphous regions, which, based on the above AFM and EQCM-D data, must be considerable. Ex situ grazing incidence small angle scattering (GISAXS) revealed a low q feature centered around $\approx 0.14 \text{ Å}^{-1}$ that appeared upon electrolyte exposure, diminished with doping, and disappeared with dedoping (Figure S14, Supporting Information). This would imply that the ion intercalation upon electrolyte exposure was heterogenous. The length scale associated with this peak ($\approx 4.5 \text{ nm}$) is smaller than the features (roughness, height) quantified with AFM, but instead similar to the coherence lengths of the BBL aggregates/crystallites. Application of a reductive potential to dope the films leads to a decrease of this peak, indicating homogeneously distributed dopant ions throughout the film. De-doping the film leads to a disappearance of the peak. As AFM and QCM-D evidence irreversible swelling, we postulate this finding to arise from trapped electrolyte. In light of the very large increases in BBL film thickness and mass upon doping, it is astonishing

that the molecular packing would be so well preserved. On the other hand, P-90 showed more significant changes in thin film structure upon electrolyte exposure and electrochemical doping (Figure S13, Supporting Information). The largest effect is the suppression of out-of-plane lamellar scattering into the background scattering, implying a disruption to the edge-on oriented crystallites (Figure S13b, Supporting Information).

Quantitative fitting of the BBL and P-90 persisting peaks yielded peak positions and coherence length estimates from the peak breadths as summarized in Table 2. Comparing the BBL and P-90 lamellar and π -stack peaks, we see that order—as estimated by coherence length—was maintained or increased in BBL upon ex situ electrolyte exposure, electrochemical doping, or electrochemical dedoping. P-90 lamellar and π -stack coherence lengths were diminished slightly by ex situ electrolyte exposure or electrochemical doping. For instance, the electrochemically doped BBL (010) coherence length increases 9% over the as cast film, while the electrochemically doped P-90 (010) coherence length decreases 15%. Further, the 3.51 Å BBL π -stack is tighter than the 3.82 Å P-90 π -stack, and unlike P-90, BBL π -stack further contracts when doped. A tighter π -stack is generally correlated with improved charge transport, as is edge-on orientation with π -stacking occurring in the plane of charge transport. As opposed to the lamellar and π -stacking, the P-90 backbone order is not disrupted by ex situ electrolyte exposure or electrochemical doping. While such order is beneficial for charge transport in undoped field effect devices,^[43] the degree of charge carrier localization likely inhibits intra-chain transport down the backbone that would benefit from this extended order.^[44] This is opposed to BBL which shows evidence of delocalized charge carriers.^[31]

3. Discussion

Our OECT characterization demonstrates that BBL performs significantly better than P-90 due to the higher electronic mobility and volumetric capacitance. In the absence of side-chains, the amount of space that is taken up by the conjugated backbone is larger, which increased BBL's charge storage

Table 2. BBL and P-90 d-spacings and coherence lengths.

hkl	BBL		P-90			
	(010)	(100)	(010)	(100)	(001)	(001)'
Orientation	In-plane	Out-of-plane	Out-of-plane	In-plane	In-plane	In-plane
neat d [Å]	3.51	8.14	3.82	25.45	13.78	7.03
Exposed d [Å]	3.51	8.26	3.81	25.48	13.80	7.03
Doped d [Å]	3.45	8.23	3.81	25.69	13.82	7.04
De-doped d [Å]	3.50	8.29	—	—	—	—
Neat L_c [Å]	39.8	29.4	50.0 (16.5) ^{a)}	106.6	210.4	191.7
Exposed L_c [Å]	46.7	30.0	47.5 (15.2) ^{a)}	91.7	215.0	199.4
Doped L_c [Å]	43.2	29.3	42.6 (15.4) ^{a)}	93.4	210.4	200.9
De-doped L_c [Å]	42.4	30.0	—	—	—	—

^{a)}The asymmetric nature of the P-90 out-of-plane (010) π -stack feature required a combination of two peaks to fit adequately, both showed peak broadening upon electrolyte exposure and doping compared to the neat as cast films.

capacity to almost triple that of P-90. Here, the unexpected result is the ion penetration and transport in a film like BBL. Previous studies suggested that for a high C^* value, the material requires a hydrophilic component to accommodate ionic conduction, which, in the case of P-90, is the EG side-chains. Giovannitti et al. demonstrated that changing the hydrophilic fraction can be used to tune μ_{OECT} and C^* of n-type films, but improving one came at the cost of the other.^[14] BBL has no such obvious hydrophilic component and appears to bypass the trade-off between μ_{OECT} and C^* parameters.

Considering high C^* and low reduction onsets, it is clear that cations have no barrier to penetrate the BBL film and couple with electrons therein. Once cations find their electron pairs, the higher mobility of BBL thus comes as no surprise, as the chain planarity, packing, and orientation are optimal for lateral electronic transport. The advantageous combination of edge-on packing, tight π -stacking, electrolyte and electrochemical doping induced order improvement, and charge carrier delocalization in BBL films, all would facilitate charge transport. P-90, on the other hand, has the disadvantageous combination of face-on packing, electrolyte and electrochemical doping induced disorder, and charge carrier localization.

Hydrophilic side chains offer a simple means of enhancing ionic conductivity within a polymer film. Side chain engineering can also promote solubility in common organic solvents and, as such, provide flexibility in processing. However, side chains may also hinder the self-assembly of chains into highly electronically conducting structures and lead to disruption of crystalline regions during doping. Our GIWAXS studies suggest a preserved backbone architecture and tighter π -stacking for BBL despite excessive swelling upon doping as shown by EQCM-D and in situ AFM studies. Doping, on the other hand, disrupts edge-on oriented crystallites and increases lamellar and π -stack coherence lengths for P-90. Our previous studies showed that excessive water uptake irreversibly distorts polymer morphology, which diminishes the electronic mobility.^[26] Ginger and colleagues hypothesized that water intercalating in the amorphous regions causes swelling and disrupts the connectivity between the crystalline regions.^[25] For P-90, we estimated more water dragged into the film for the same amount of dopant ions. In contrast to BBL, the amorphous content and bulky EG chains that attract water makes P-90's structure and electron transport pathways more vulnerable to ion induced swelling.

BBL chains exhibit large persistence lengths of up to ≈ 153 nm (limited by the overall chain length),^[45] whereas the persistence length of the NDI-T2 backbone appears to be limited to ≈ 26 nm, regardless of the overall chain length.^[46] We suggest that rigid long chains of BBL extend across amorphous regions connecting multiple crystallites. Although dry AFM and TEM images showed no porosity for BBL in the length scales that we could investigate, we postulate that these intercrystallite disordered regions have enough void space to allow electrolyte intercalation, as evidenced by GISAXS. The rigid-chain architecture maintains the integrity of electron conduction pathways despite swelling and ion uptake. In P-90, on the other hand, ions interact with EG side chains and water, especially in the swollen amorphous regions, disrupting crystallite connectivity necessary for efficient charge transport.

4. Conclusions

We demonstrated that the ladder-type polymer BBL outperforms the NDI-T2 based glycolated P-90 random copolymer as the OECT channel material. By employing frequency dependent measurements, we found that the electronic OECT mobility of BBL is ≈ 28 times and its volumetric capacitance is ≈ 2.8 times higher than that of P-90. Because BBL does not have any hydrophilic side-chains, one would expect lower electrolyte affinity and lower ion-electron coupling capability in aqueous environments, as seen in alkylated NDI-T2 derivatives. However, both EQCM-D and UV-vis spectroscopy demonstrated that BBL has an earlier reduction onset and facilitates a higher degree of swelling upon electrochemical reduction and electrochromic response compared to P-90. BBL accommodated a higher density of cations and water during its electrochemical reduction, which remained partially in the film upon dedoping. On the other hand, the water-to-cation ratio was higher for P-90. In situ AFM images showed that during doping, the feature size and surface roughness of BBL increases drastically and abruptly, compared to the more gradual and modest changes seen in P-90, in agreement with EQCM-D results. GIWAXS studies showed that electrolyte uptake in the BBL film during doping did not disrupt molecular packing, which is not the case for P-90. We hypothesize that the structural resistance to water originates from the planarity of BBL chains and lack of ion-coordinating side-chains. This architecture provides efficient transport routes for electronic carriers, while permitting electrolyte intercalation in intermolecular void space. BBL should be considered as a new model system for the design of mixed conductors since this rigid-backbone, side chain-free route results in the highest ever n-type OECT performance and efficient mixed conduction at the aqueous electrolyte interface.

5. Experimental Section

Materials: P-90 was synthesized using an existing protocol.^[14] BBL was purchased from Sigma Aldrich and used as received.

Device Preparation: OECTs were fabricated using an established photolithography process on 4-inch glass wafers. The wafers were cleaned using a piranha ($\text{H}_2\text{O}_2\text{:H}_2\text{SO}_4$, ratio 1:3–4) bath, washed with water and cleaned with O_2 plasma (Nanoplas DSB 6000). The OECT components (channels, pads, and interconnects) were defined using standard photolithography steps. To perform the lift-off step, the wafers were coated with a photoresist bilayer consisting of LOR 5B (Microchem) and S1813 (Shipley), and exposed to UV light using the EVG 6200 mask alignment system and developed using MF319 developer. A 10 nm layer of Cr and a 100 nm layer of Au were deposited using magnetron sputtering (Equipment Support Company Ltd. ESCRD4) and lifted using appropriate solvents. After the lift-off step, the first Parylene C layer was vaporized to a thickness of $1.7\ \mu\text{m}$ using a SCS Labcoater 2 with Silane as an adhesion promoter. A second Parylene C layer was vaporized to act as the sacrificial layer for polymer film patterning. A layer of AZ9260 was spun cast and developed using AZ developer as a mask for reactive ion etching (Oxford Instruments Plasmalab 100–ICP 380) which was used to expose the device channels and pads for polymer deposition. P-90 was prepared in a chloroform solution, while BBL was prepared in a methanesulfonic acid (MSA) solution, keeping a $5\ \text{mg}\cdot\text{mL}^{-1}$ concentration for both polymer solutions. P-90 films were spin-coated at 1500 rpm, for 30 s. BBL films were spin-coated using a two-step process: 1000 rpm for 60 s, during which the films settled and 3000 rpm for 15 s to remove excess solution. After spin-coating, the BBL films were

immersed in DI water for 30 min to remove MSA from the film. The films were then annealed at 200 °C for 1 h.

Device Characterization: A Keithley source-meter unit and a dual-channel source-meter unit (NI-PXI) with custom-written LabView control codes were used for OECT characterization. An Ag/AgCl pellet (2 mm × 2 mm, Warner instruments) was used as the gate electrode, immersed into aqueous 0.1 M NaCl solution contained in a PDMS well placed on top of the OECTs. To find the electron transit time (τ_e) and the electronic mobility (μ_{e-OECT}), transconductance frequency response measurements were performed as described by Rivnay et al.^[34] A constant drain voltage ($V_D = 0.6$ V) and gate voltage ($V_G = 0.6$ or 0.5 V) along with a sinusoidal gate voltage modulation ($\Delta V_G = 50$ mV) was applied over a frequency range from 1 Hz to 20 kHz. The gate current (I_G) and drain current (I_D) as well as the associated amplitude and phase shift responses were collected and analyzed with a custom-made LabView code. The frequency domain relation between I_G and I_D can be described as:

$$\Delta I_G(f) = 2\pi f \tau_e \Delta I_D(f) \quad (2)$$

The electron transit time τ_e was extracted using a frequency matching MATLAB script. The electronic mobility was calculated using the relation described by the Bernard's model:

$$\mu_{OECT} = \frac{L^2}{\tau_e V_D} \quad (3)$$

where L is the channel length, τ_e is the extracted electron transit time, and V_D is the drain voltage applied.^[33]

Electrochemical Analysis: Cyclic voltammograms were measured using a Metrohm Autolab potentiostat using the standard three-electrode setup at a 50 mV s⁻¹ scan rate in air or in a N₂-filled glovebox. The polymer films spin-coated on gold substrates (2 × 2 cm) acted as the working electrodes, with a platinum wire as the counter electrode and an Ag/AgCl as the reference electrode. A 0.7 mm diameter PDMS well was used to contain the 300 μL of NaCl(aq), into which the counter and reference electrodes were immersed. EIS was performed on microelectrode arrays with Au electrodes coated with the polymers. The sizes of these microelectrodes ranged from 400 to 94 950 μm² and were patterned using photolithography as described for the OECTs above. A Metrohm Autolab potentiostat over a frequency range from 100 kHz to 0.1 Hz with a 10 mV modulation amplitude was used. Capacitances were calculated from the impedance magnitude equation:

$$|Z| = \sqrt{R^2 + X_C^2} \quad (4)$$

where Z is the complex impedance, R is the real resistance component, and X_C is the imaginary reactance component, from which capacitance can be expressed as:

$$C = \frac{1}{2\pi f X_C} \quad (5)$$

where C is the capacitance and f is frequency. Volumetric capacitance was obtained from the slope of the extracted capacitance versus film volume curve.

Spectroelectrochemical Analysis: Measurements were performed using an Ocean Optics HL-2000-FHSA halogen light source, directed through a redox.me sample holder (MM SPECTRO-EFC) using QP600-1-SR-BX optical fibers and fed back to the Ocean Optics QE65 Pro Spectrometer. The OceanView software was first calibrated using a blank ITO substrate placed in the sample holder. The polymers films were spin-coated on ITOs and placed into the sample holder in direct contact with 1.3 mL of NaCl(aq) 0.1 M. A Keithley 2602A source meter was connected to the ITO surface and an Ag/AgCl electrode (redox.me—Ag/AgCl 30 mm) which was inserted into the electrolyte. The samples were electrochemically cycled using the Keithley source-meter unit, which provided a ramp voltage from 0.2 to -0.9 V (vs Ag/AgCl) with a 0.1 V step for a duration of 5 min. Absorbance was recorded automatically using the OceanView software.

Electrochemical Quartz Crystal Microbalance with Dissipation Monitoring: Measurements were performed using the QSense Analyzer, a QSense Electrochemistry Module (QEM 401), and gold with titanium adhesion layer sensors (QSensors QX 338) from Biolin Scientific in deoxygenated electrolytes bubbled continuously with argon gas. The analyzer measured the shift and dissipation of the 1st, 3rd, 5th, 7th, 9th, and 11th frequency harmonics which provide information about the changes in sample mass and softness. First, the bare sensors were measured in air and after introducing NaCl(aq) 0.1 M. The electrolyte resulted in a large shift in the QCM-D signals due to the change in media density inside the chamber, which needs to be taken into consideration when calculating polymer swelling. After acquiring QCM-D baseline signals in both dry and wet conditions, the measured sensor was coated with a polymer film and placed back into the analyzer. The QCM-D signals were recorded again in dry state and with electrolyte after making sure that the f and D signals were stabilized (i.e., $\Delta f < 0.1$ Hz per 5 min). Using the QSoft software function "stitch data" provided the difference between the f and D signals before and after the sensor was coated with a polymer film in both dry state and with electrolyte. This difference was used to calculate the film areal mass in dry and swollen states, using the Sauerbrey equation:

$$\frac{\Delta m}{A} = -\Delta f_n \frac{\rho_q V_q}{2f_0^2 n} \approx \frac{-\Delta f_n}{n} 17.9 \text{ ng cm}^{-2} \quad (6)$$

where Δf_n is the frequency shift of the n th overtone, A is the sensor active area, ρ_q is the density of quartz, V_q is the shear wave velocity in quartz, f_0 is the fundamental frequency and n is the overtone number. Film thickness was calculated by dividing the calculated areal mass with film density.

EQCM-D was performed using an Autolab PGstat128N potentiostat coupled with a QSense electrochemistry module (QEM 401). The integrated three-electrode setup comprised a Ag/AgCl reference electrode, Pt counter electrode, and the polymer-coated Au QSensor acting as the working electrode with an electrochemical active area of 0.7854 cm².

Physical modeling of the measured f and D signals was done based on observed film characteristics. Films exhibiting a low degree of swelling and little to no energy losses were considered "rigid" and modeled using the Sauerbrey equation.

Swelling in Figure 2 and Figure S2, Supporting Information was calculated as the percentage change in volume relative to the dry volume:

$$\text{swelling}_{\text{total}} = \frac{Vol_{\text{total}} - Vol_{\text{dry}}}{Vol_{\text{dry}}} * 100\% \quad (7)$$

Na⁺ density was determined by calculating the number of electrons injected into the polymer film from the recorded working electrode current and assuming a 1:1 electron-to-cation coupling. H₂O density was determined by subtracting the injected Na⁺ mass (3.81763×10^{-23} g per atom) from the total electrochemically injected mass and dividing by water molecular mass (2.99158×10^{-23} g per molecule). Possible contributions of counter ions or faradaic reactions on mass uptake and measured current were not considered.

The injected charge density was calculated from the working electrode current and the corresponding Na⁺ mass density was obtained using Faraday's law of electrolysis:

$$m = \frac{QM_{Na^+}}{Fn} \quad (8)$$

where m is the mass of injected Na⁺ ions, Q is charge injected from the working electrode, M_{Na^+} is the atomic mass of Na⁺, F is the Faraday constant, n is the valency number of Na⁺ (i.e., 1).

Atomic Force Microscopy: Scans obtained with a Veeco Dimension 3100 Scanning Probe System. Dry films experiments were performed with spin

coated films on ITO using FESPA-V2 probes commercialized by Bruker (nominal resonant frequency: 75 KHz, spring constant: 2.8 N m^{-1}). In electrolyte scans were obtained using the Bruker SCANASYST-FLUID module mounted with Scanasyt-fluid probes commercialized by Bruker (nominal resonant frequency: 150 KHz, spring constant: 0.7 N m^{-1}). Sample and probe were both immersed in PBS while scanning. Doping of the film was achieved in PBS with a two-electrode set up, the film spin coated on ITO and an Ag/AgCl pellet were connected to a potentiostat (PalmSens, PalmSens4). Doping of the film was performed applying the desired voltage versus an Ag/AgCl reference for at least 10 min. Scans were taken immediately after doping. Preparation of the films was consistent with the other experiments (P-90: 1500 rpm for 30 s; BBL: 1000 rpm for 1 min then 3000 rpm for 15 s). Gwyddion software was used for statistical data and post-treatment.

Transmission Electron Microscopy: BBL and P-90 films were spin-coated onto glass substrates using the same conditions as in other experiments. Both films were floated onto DI water and transferred onto TEM grids (Agar Scientific 200 mesh copper, Formvar/Carbon). BBL covered grids were annealed at 200°C for 1 h. The P-90 and BBL films' morphology were investigated by bright-field imaging on FEI TECNAI G2 SPIRIT TWIN TEM operated at 100 kV with Gatan ultra-scan CCD camera.

Grazing Incidence Wide Angle X-Ray Scattering GIWAXS measurements were performed at beamline 8-ID-E of the Advanced Photon Source, Argonne National Laboratory with 10.92 keV synchrotron radiation, an incident angle of 0.14° , under vacuum at room temperature, with images collected by a Pilatus 1M pixel array detector 228.165 mm away from the sample. BBL films for GIWAXS were prepared by: spin-coating and drying (pristine); spin-coating, drying, exposing to $0.1 \text{ M NaCl}_{(\text{aq})}$ for 30 min, and drying (exposed); spin-coating, drying, exposing to $0.1 \text{ M NaCl}_{(\text{aq})}$ for 30 min, doping at -0.6 V (vs Ag/AgCl) for 30 min, and drying (doped); spin-coating, drying, exposing to $0.1 \text{ M NaCl}_{(\text{aq})}$ for 30 min, doping at -0.6 V (vs Ag/AgCl) for 30 min, dedoping at 0 V (vs Ag/AgCl) for 30 min, and drying (de-doped). Data were processed with the GIXSGUI package for MATLAB,^[47] and line cuts were fit with custom MATLAB code.

Supporting Information

Supporting Information is available from the Wiley Online Library or from the author.

Acknowledgements

The research reported in this publication was supported by funding from KAUST, Office of Sponsored Research (OSR), under award number OSR-2016-CRG5-3003, URF/1/4073-01 and OSR-2018-CRG7-3709. J. S. thanks Dr. Yi Zhang for the TEM image of P-90. B.D.P., R.W., and J.R. gratefully acknowledge support from the National Science Foundation Grant No. NSF DMR-1751308. This research used resources of the Advanced Photon Source, a U.S. Department of Energy (DOE) Office of Science User Facility operated for the DOE Office of Science by Argonne National Laboratory under Contract No. DE-AC02-06CH11357. The authors would like to thank Joseph Strzalka and Qingteng Zhang for beam line assistance.

Conflict of Interest

The authors declare no conflict of interest.

Data Availability Statement

The data that supports the findings of this study are available in the supplementary material of this article.

Keywords

capacitance, in operando, n-type, organic electrochemical transistors, organic mixed conductors

Received: November 26, 2020

Revised: February 10, 2021

Published online: March 18, 2021

- [1] J. Rivnay, S. Inal, A. Salleo, R. M. Owens, M. Berggren, G. G. Malliaras, *Nat. Rev. Mater.* **2018**, 3, 17086.
- [2] M. Moser, J. F. Ponder Jr., A. Wadsworth, A. Giovannitti, I. McCulloch, *Adv. Funct. Mater.* **2019**, 29, 1807033.
- [3] D. Ohayon, S. Inal, *Adv. Mater.* **2020**, 32, 2001439.
- [4] D. Khodagholy, T. Doublet, P. Quilichini, M. Gurfinkel, P. Leleux, A. Ghestem, E. Ismailova, T. Hervé, S. Sanaur, C. Bernard, G. G. Malliaras, *Nat. Commun.* **2013**, 4, 1575.
- [5] A. M. Pappa, D. Ohayon, A. Giovannitti, I. P. Maria, A. Savva, I. Uguz, J. Rivnay, I. McCulloch, R. M. Owens, S. Inal, *Sci. Adv.* **2018**, 4, eaat0911.
- [6] D. Ohayon, G. Nikiforidis, A. Savva, A. Giugni, S. Wustoni, T. Palanisamy, X. Chen, I. P. Maria, E. Di Fabrizio, P. M. F. J. Costa, I. McCulloch, S. Inal, *Nat. Mater.* **2019**, 19, 456.
- [7] Y. van de Burgt, E. Lubberman, E. J. Fuller, S. T. Keene, G. C. Faria, S. Agarwal, M. J. Marinella, A. Alec Talin, A. Salleo, *Nat. Mater.* **2017**, 16, 414.
- [8] P. Andersson Ersman, R. Lassnig, J. Strandberg, D. Tu, V. Keshmiri, R. Forchheimer, S. Fabiano, G. Gustafsson, M. Berggren, *Nat. Commun.* **2019**, 10, 5053.
- [9] C. B. Nielsen, A. Giovannitti, D.-T. Sbircea, E. Bandiello, M. R. Niazi, D. A. Hanifi, M. Sessolo, A. Amassian, G. G. Malliaras, J. Rivnay, I. McCulloch, *J. Am. Chem. Soc.* **2016**, 138, 10252.
- [10] A. Giovannitti, K. J. Thorley, C. B. Nielsen, J. Li, M. J. Donahue, G. G. Malliaras, J. Rivnay, I. McCulloch, *Adv. Funct. Mater.* **2018**, 28, 1706325.
- [11] L. R. Savagian, A. M. Österholm, J. F. Ponder Jr., K. J. Barth, J. Rivnay, J. R. Reynolds, *Adv. Mater.* **2018**, 30, 1804647.
- [12] A. Giovannitti, D.-T. Sbircea, S. Inal, C. B. Nielsen, E. Bandiello, D. A. Hanifi, M. Sessolo, G. G. Malliaras, I. McCulloch, J. Rivnay, *Proc. Natl. Acad. Sci. U. S. A.* **2016**, 113, 12017.
- [13] A. Giovannitti, C. B. Nielsen, D.-T. Sbircea, S. Inal, M. Donahue, M. R. Niazi, D. A. Hanifi, A. Amassian, G. G. Malliaras, J. Rivnay, I. McCulloch, *Nat. Commun.* **2016**, 7, 13066.
- [14] A. Giovannitti, I. P. Maria, D. Hanifi, M. J. Donahue, D. Bryant, K. J. Barth, B. E. Makdah, A. Savva, D. Moia, M. Zetek, P. R. F. Barnes, O. G. Reid, S. Inal, G. Rumbles, G. G. Malliaras, J. Nelson, J. Rivnay, I. McCulloch, *Chem. Mater.* **2018**, 30, 2945.
- [15] H. Sun, J. Gerasimov, M. Berggren, S. Fabiano, *J. Mater. Chem. C* **2018**, 6, 11778.
- [16] A. Savva, D. Ohayon, J. Surgailis, A. F. Paterson, T. C. Hidalgo, X. Chen, I. P. Maria, B. D. Paulsen, A. J. Petty II, J. Rivnay, I. McCulloch, S. Inal, *Adv. Electron. Mater.* **2019**, 5, 1900249.
- [17] A. F. Paterson, A. Savva, S. Wustoni, L. Tsetseris, B. D. Paulsen, H. Faber, A. H. Emwas, X. Chen, G. Nikiforidis, T. C. Hidalgo, M. Moser, I. P. Maria, J. Rivnay, I. McCulloch, T. D. Anthopoulos, S. Inal, *Nat. Commun.* **2020**, 11, 3004.
- [18] M. Kawan, T. C. Hidalgo, W. Du, A.-M. Pappa, R. M. Owens, I. McCulloch, S. Inal, *Mater. Horiz.* **2020**, 7, 2348.
- [19] D. Moia, A. Giovannitti, A. A. Szumska, I. P. Maria, E. Rezasoltani, M. Sachs, M. Schnurr, P. R. F. Barnes, I. McCulloch, J. Nelson, *Energy Environ. Sci.* **2019**, 12, 1349.
- [20] H. Sun, M. Vagin, S. Wang, X. Crispin, R. Forchheimer, M. Berggren, S. Fabiano, *Adv. Mater.* **2018**, 30, 1704916.

- [21] B. A. Jones, A. Facchetti, M. R. Wasielewski, T. J. Marks, *J. Am. Chem. Soc.* **2007**, 129, 15259.
- [22] X. Zhan, A. Facchetti, S. Barlow, T. J. Marks, M. A. Ratner, M. R. Wasielewski, S. R. Marder, *Adv. Mater.* **2011**, 23, 268.
- [23] M. Goel, C. D. Heinrich, G. Krauss, M. Thelakkat, *Macromol. Rapid Commun.* **2019**, 40, 1800915.
- [24] R. Di Pietro, D. Fazzi, T. B. Kehoe, H. Sirringhaus, *J. Am. Chem. Soc.* **2012**, 134, 14877.
- [25] L. Q. Flagg, C. G. Bischak, J. W. Onorato, R. B. Rashid, C. K. Luscombe, D. S. Ginger, *J. Am. Chem. Soc.* **2019**, 141, 4345.
- [26] A. Savva, C. Cendra, A. Giugni, B. Torre, J. Surgailis, D. Ohayon, A. Giovannitti, I. McCulloch, E. Di Fabrizio, A. Salleo, J. Rivnay, S. Inal, *Chem. Mater.* **2019**, 31, 927.
- [27] A. Savva, R. Hallani, C. Cendra, J. Surgailis, T. C. Hidalgo, S. Wustoni, R. Sheelamantula, X. Chen, M. Kirkus, A. Giovannitti, A. Salleo, I. McCulloch, S. Inal, *Adv. Funct. Mater.* **2020**, 30, 1907657.
- [28] Y. Wang, E. Zeglio, H. Liao, J. Xu, F. Liu, Z. Li, I. P. Maria, D. Mawad, A. Herland, I. McCulloch, W. Yue, *Chem. Mater.* **2019**, 31, 9797.
- [29] M. Moser, T. C. Hidalgo, J. Surgailis, J. Gladisch, S. Ghosh, R. Sheelamantula, Q. Thiburce, A. Giovannitti, A. Salleo, N. Gasparini, A. Wadsworth, I. Zozoulenko, M. Berggren, E. Stavrinidou, S. Inal, I. McCulloch, *Adv. Mater.* **2020**, 32, 2002748.
- [30] M. ElMahmoudy, S. Inal, A. Charrier, I. Uguz, G. G. Malliaras, S. Sanaur, *Macromol. Mater. Eng.* **2017**, 302, 1600497.
- [31] S. Wang, H. Sun, U. Ail, M. Vagin, P. O. Å. Persson, J. W. Andreasen, W. Thiel, M. Berggren, X. Crispin, D. Fazzi, S. Fabiano, *Adv. Mater.* **2016**, 28, 10764.
- [32] A. Savva, S. Wustoni, S. Inal, *J. Mater. Chem. C* **2018**, 6, 12023.
- [33] D. A. Bernards, G. G. Malliaras, *Adv. Funct. Mater.* **2007**, 17, 3538.
- [34] J. Rivnay, M. Ramuz, P. Leleux, A. Hama, M. Huerta, R. M. Owens, *Appl. Phys. Lett.* **2015**, 106, 043301.
- [35] Y. Zhang, A. Savva, S. Wustoni, A. Hama, I. P. Maria, A. Giovannitti, I. McCulloch, S. Inal, *ACS Appl. Bio Mater.* **2018**, 1, 1348.
- [36] M. Quinto, S. A. Jenekhe, A. J. Bard, *Chem. Mater.* **2001**, 13, 2824.
- [37] A. Babel, S. A. Jenekhe, *J. Am. Chem. Soc.* **2003**, 125, 13656.
- [38] A. L. Briseno, F. S. Kim, A. Babel, Y. Xia, S. A. Jenekhe, *J. Mater. Chem.* **2011**, 21, 16461.
- [39] J. Rivnay, M. F. Toney, Y. Zheng, I. V. Kauvar, Z. Chen, V. Wagner, A. Facchetti, A. Salleo, *Adv. Mater.* **2010**, 22, 4359.
- [40] T. Schuettfort, S. Huettner, S. Lilliu, J. E. Macdonald, L. Thomsen, C. R. McNeill, *Macromolecules* **2011**, 44, 1530.
- [41] J. Rivnay, R. Steyrleuthner, L. H. Jimison, A. Casadei, Z. Chen, M. F. Toney, A. Facchetti, D. Neher, A. Salleo, *Macromolecules* **2011**, 44, 5246.
- [42] A. L. Briseno, S. C. B. Mannsfeld, P. J. Shamberger, F. S. Ohuchi, Z. Bao, S. A. Jenekhe, Y. Xia, *Chem. Mater.* **2008**, 20, 4712.
- [43] K. Tremel, F. S. U. Fischer, N. Kayunkid, R. D. Pietro, R. Tkachov, A. Kiri, D. Neher, S. Ludwigs, M. Brinkmann, *Adv. Energy Mater.* **2014**, 4, 1301659.
- [44] I. Denti, S. Cimò, L. Brambilla, A. Milani, C. Bertarelli, M. Tommasini, C. Castiglioni, *Chem. Mater.* **2019**, 31, 6726.
- [45] G. C. Berry, *J. Polym. Sci., C Polym. Symp.* **1978**, 65, 143.
- [46] L. A. Galuska, W. W. McNutt, Z. Qian, S. Zhang, D. W. Weller, S. Dhakal, E. R. King, S. E. Morgan, J. D. Azoulay, J. Mei, X. Gu, *Macromolecules* **2020**, 53, 6032.
- [47] Z. Jiang, *J. Appl. Crystallogr.* **2015**, 48, 917.